Fatigue performance of auxetic meta-biomaterials

Kolken, H. M.A.; Garcia, A. Fontecha; Du Plessis, A.; Rans, C.; Mirzaali, M. J.; Zadpoor, A. A.

DOI
10.1016/j.actbio.2021.03.015

Publication date
2021

Document Version
Final published version

Published in
Acta Biomaterialia

Citation (APA)
Kolken, H. M. A., Garcia, A. F., Du Plessis, A., Rans, C., Mirzaali, M. J., & Zadpoor, A. A. (2021). Fatigue performance of auxetic meta-biomaterials. *Acta Biomaterialia*, *126*, 511-523. https://doi.org/10.1016/j.actbio.2021.03.015

Acta Biomaterialia 126 (2021) 511–523

Contents lists available at ScienceDirect

Acta Biomaterialia

journal homepage: www.elsevier.com/locate/actbio

Full length article

Fatigue performance of auxetic meta-biomaterials

H.M.A. Kolken[a,*], A. Fontecha Garcia[b], A. Du Plessis[c], C. Rans[d], M.J. Mirzaali[a], A.A. Zadpoor[a]

[a] Department of Biomechanical Engineering, Delft University of Technology, Delft, Netherlands
[b] 3D Systems – LayerWise NV, Leuven, Belgium
[c] Research group 3D Innovation, Stellenbosch University, Stellenbosch, South-Africa
[d] Department of Aerospace Structures and Materials, Delft University of Technology, Delft, Netherlands

ARTICLE INFO

Article history:
Received 22 January 2021
Revised 4 March 2021
Accepted 4 March 2021
Available online 9 March 2021

Keywords:
Auxetics
Meta-biomaterials
Fatigue
Cyclic loading
Additive manufacturing

ABSTRACT

Meta-biomaterials offer a promising route towards the development of life-lasting implants. The concept aims to achieve solutions that are ordinarily impossible, by offering a unique combination of mechanical, mass transport, and biological properties through the optimization of their small-scale geometrical and topological designs. In this study, we primarily focus on auxetic meta-biomaterials that have the extraordinary ability to expand in response to axial tension. This could potentially improve the longstanding problem of implant loosening, if their performance can be guaranteed in cyclically loaded conditions. The high-cycle fatigue performance of additively manufactured (AM) auxetic meta-biomaterials made from commercially pure titanium (CP-Ti) was therefore studied. Small variations in the geometry of the re-entrant hexagonal honeycomb unit cell and its relative density resulted in twelve different designs (relative density: ~5–45%, re-entrant angle = 10–25°, Poisson's ratio = -0.076 to -0.504). Micro-computed tomography, scanning electron microscopy and mechanical testing were used to respectively measure the morphological and *quasi-static* properties of the specimens before proceeding with compression-compression fatigue testing. These auxetic meta-biomaterials exhibited morphological and mechanical properties that are deemed appropriate for bone implant applications (elastic modulus = 66.3–5648 MPa, yield strength = 1.4–46.7 MPa, pore size = 1.3–2.7 mm). With an average maximum stress level of 0.47 σ_y at 10^6 cycles (range: 0.35 $\sigma_y\sigma_y$- 0.82 $\sigma_y\sigma_y$), the auxetic structures characterized here are superior to many other non-auxetic meta-biomaterials made from the same material. The optimization of the printing process and the potential application of post-processing treatments could improve their performance in cyclically loaded settings even further.

Statement of Significance

Auxetic meta-biomaterials have a negative Poisson's ratio and, therefore, expand laterally in response to axial tension. Recently, they have been found to restore bone-implant contact along the lateral side of a hip stem. As a result, the bone will be compressed along both of the implant's contact lines, thereby actively reducing the risk of implant failure. In this case the material will be subjected to cyclic loading, for which no experimental data has been reported yet. Here, we present the first ever study of the fatigue performance of additively manufactured auxetic meta-biomaterials based on the re-entrant hexagonal honeycomb. These results will advance the adoption of auxetic meta-biomaterials in load-bearing applications, such as the hip stem, to potentially improve implant longevity.

1. Introduction

The innovative design of orthopedic implants can play a major role in the improvement of their long-term performance. Total joint replacements are still considered one of the most suc-

* Corresponding author.
E-mail address: h.m.a.kolken@tudelft.nl (H.M.A. Kolken).

https://doi.org/10.1016/j.actbio.2021.03.015

cessful surgical interventions, but the increasing prevalence of osteoarthritis among younger patients calls for a unique, improved approach [1,2]. Meta-biomaterials are multi-physics metamaterials whose geometry and topology are architected to provide an unusual combination of mechanical, mass transport, and biological properties [3–5]. Advances in additive manufacturing (AM) have opened up new possibilities for the production of such complex micro-architectures.

Here, we will primarily focus on auxetic meta-biomaterials, which exhibit a negative Poisson's ratio [6]. In contrast to conventional materials, these materials expand in response to axial tension. In a previous study, the concept of combining conventional and auxetic meta-biomaterials to design a hip stem was presented [5]. With the application of a negative Poisson's ratio on the lateral side of the implant, compression was created along both of the implant's contact lines with the surrounding bone. As a consequence of compressive loading, the risk of failure at the implant-bone interface is reduced. Moreover, bone will be actively remodeled according to Wolff's law, thereby enhancing bony ingrowth, strengthening the implant-bone interface, and improving the implant longevity [5,7].

For such load-bearing applications in which the material is subjected to cyclic loading, it is important to study the fatigue behavior of AM meta-biomaterials [8]. There is currently only limited data available regarding the fatigue performance of auxetic structures [9,10]. A comparison between auxetic and non-auxetic structures has shown that the re-entrant hexagonal honeycomb may exhibit superior fatigue strength [9,11]. Additionally, auxetic foams have been found to exhibit enhanced energy dissipation behavior and dynamic crushing performance as compared to non-auxetic foams [12,13]. Despite the availability of such isolated studies, there is no experimental data available on the high-cycle fatigue behavior of AM auxetic meta-biomaterials based on the re-entrant hexagonal honeycomb unit cell and built from biocompatible metals.

We, therefore, studied the compression-compression fatigue behavior of directly printed auxetic meta-biomaterials made from commercially pure titanium (CP-Ti). Their potential as bone-substitutes was proven in a recent study on the *quasi-static* mechanical properties of auxetic meta-biomaterials made from Ti-6Al-4V [14]. Despite its good biocompatibility and high strength-to-weight ratio, Ti-6Al-4V is quite brittle and contains several hazardous alloying components [15,16]. CP-Ti, on the other hand, is very ductile. According to Wauthle et al. (2015), CP-Ti is a competitive biomaterial for the fabrication of load-bearing orthopedic implants [17]. That is partially due to its high ductility, which helps in slowing down both crack initiation and crack propagation processes. Due to these advantages, CP-Ti was selected for the first ever study of the fatigue performance of AM auxetic metallic meta-biomaterials.

Since the dominant mode of musculoskeletal loading is compression, many studies have evaluated the compression-compression fatigue behavior of bone-mimicking porous structures [17–22]. The same loading regime was chosen here. Prior to fatigue tests, a thorough morphological characterization was performed using scanning electron microscopy (SEM) and micro-computed tomography (micro-CT). The morphological characterizations were followed by uniaxial compression tests, which were used to measure the *quasi-static* mechanical properties of the specimens.

2. Materials and methods

2.1. Design and additive manufacturing of auxetic meta-biomaterials

The negative Poisson's ratio of auxetic meta-biomaterials based on the re-entrant unit cells depends on several geometrical parameters, such as the re-entrant angle (θ) and rib-length ratio (a/b) [6,14]. Based on the data published earlier [14], four unit cell types (A-D) were chosen (Fig. 1). The re-entrant hexagonal honeycomb was implemented with an aspect ratio of 1.0 and 1.5, each combined with two different re-entrant angles (10, 15, 20, and 25°, respectively) and a uniform cell height of 2.5 mm. These unit cell types were used to build cylindrical specimens (filling a cylinder of ∅ 25 mm and h = 37.5 mm). By varying the strut thickness, three different relative densities (≈5%, ≈25%, and ≈45% RD) were obtained. As a result, 12 different designs were prepared for production (Table 1). Based on the analytical relationships presented by Hedayati and Ghavidelnia (2020), these structures should exhibit a Poisson's ratio in the range of −0.076 to −0.504 [23].

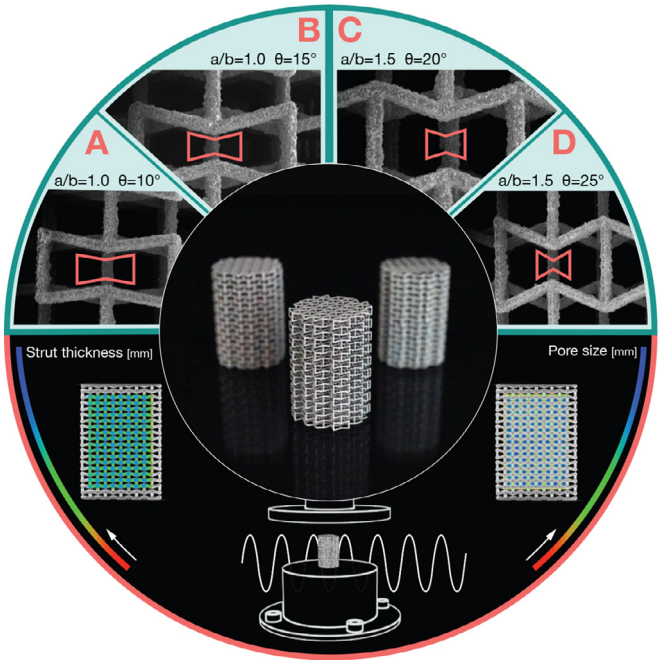

Fig. 1. The study outline showing the four different design types: A, B, C and D, the AM cylindrical specimens, and their assessment using compression-compression fatigue testing, SEM imaging, and micro-CT scanning.

All designs were directly printed using Ti Gr1 (CP-Ti) powder (3D Systems, Leuven, Belgium) (Fig. 1). The chemical composition of this specific grade of powder complies with ASTM F67, ASTM B265, ASTM B348, ISO 5832–2 and ISO 13782 standards. The samples were manufactured by laser powder bed fusion using a DMP Flex 350 machine with DMP Control Software (3D Systems, Leuven, Belgium). A layer thickness of 30 µm was used. The structures were built laying down, at a 10-degree angle with respect to the build plate, to make sure overhang structures could be printed without the need for internal supports. The down-facing side was supported along the complete length of the cylinder. For each design, 30 specimens were printed, which were manually removed from the build plate. To remove the excess powder particles, the structures were ultrasonically cleaned in 96% ethanol.

2.2. Morphological characterization

After manufacturing, the specimens were visually assessed on their print qualityqw. The structures with a relatively high density (with thicker struts) exhibited signs of warping. Consequently, the outer ends of these cylinders were no longer parallel. To make sure the compression plates were in full contact with the specimens, both ends of the cylinder were turned on a lathe. The dry weighing technique was used to determine the as-manufactured

Table 1
The designed and as-manufactured dimensions of the auxetic meta-biomaterials, designs A, B, C and D. Manual measurements have been presented as mean ± standard deviation.

Type	RD [%]	Diameter [mm]		Height [mm]		Cum. deviation [mm]
	CAD	CAD	As-manufactured	CAD	As-manufactured	Micro-CT
A	4.6	24.99	25.26 ± 0.06	35.92	35.83 ± 0.04	0.09
	24.1	25.50	25.77 ± 0.07	36.44	36.34 ± 0.07	0.09
	42.7	25.86	26.00 ± 0.07	36.79	35.89 ± 0.08	0.15
B	5.4	24.51	24.82 ± 0.05	36.22	36.12 ± 0.03	0.10
	25.4	24.99	25.20 ± 0.04	36.69	36.55 ± 0.03	0.08
	45.4	25.32	25.56 ± 0.10	37.02	35.88 ± 0.05	0.10
C	4.9	22.20	22.51 ± 0.05	35.58	35.51 ± 0.02	0.13
	24.6	22.57	22.81 ± 0.05	35.95	35.85 ± 0.05	0.11
	43.2	22.83	23.06 ± 0.06	36.21	35.09 ± 0.07	0.17
D	3.4	22.00	22.32 ± 0.05	35.57	35.50 ± 0.01	0.14
	17.5	22.34	22.59 ± 0.05	35.91	35.81 ± 0.05	0.10
	32.5	22.58	22.79 ± 0.04	36.15	35.09 ± 0.07	0.12

relative density. The outer dimensions were, therefore, measured with a caliper, while a laboratory scale (Sartorius AG, Göttingen, Germany, 0.1 mg accuracy) was used to weigh the specimens. The weight of the specimens was then divided by the weight of a solid CP-Ti object with similar dimensions and a density of 4.51 g/cm^3 [24].

Additionally, the surface morphology and print quality of the auxetic meta-biomaterials were assessed using SEM (JSM-IT100LA, JEOL, Tokyo, Japan). With a beam energy of 10–20 kV and a working distance of 25–35 mm, one specimen of each design type was scanned for assessment. The strut thickness values were obtained at 10 different locations, on either side of the specimens, resulting in 20 data points in total. The failure surfaces were studied in case the specimen broke apart, which was the case in the higher density specimens of design A and B. All specimens were photographed after fatigue failure.

Micro-CT is increasingly used for detailed three-dimensional characterizations of AM components [25]. In this study, micro-CT scanning was performed on one specimen of each design type using a Nanotom S system (GE, Boston, USA) (160 kV; 300 µA; 0.5 mm copper beam filtration). The voxel size was set to 21.88 µm to fit the entire specimen in the field of view. A total of 4000 images were recorded in a full rotation, including image averaging and detector shift to enhance the image quality. Image processing and analyses were performed in Volume Graphics VGSTUDIO MAX 3.4 (Volume Graphics GmbH, Heidelberg, Germany).

Morphological data were acquired from a cylindrical region of interest (Ø =20 mm, h = 30 mm), to eliminate the edge effects. Basic material and pore fractions were calculated using the sub-voxel accurate surface determination. The local strut and pore sizes were determined using the wall thickness analysis (sphere) method. This method fits the largest sphere in the analysis region at each location and reports this value at all locations within the structure, in the form of a statistical representation of the local thickness (Fig. 1) [26]. Recently, this method was applied to characterize lattice structures, highlighting the concept that some designs have multiple inherent pore sizes, which might be beneficial for bony growth [27]. It should be noted that the strut thickness analysis also measures the node regions, creating a bimodal distribution of thickness values. The statistical information is binned according to the local thickness across the entire structure. The same procedure was performed for the pore size analysis, giving an idea of the actual spherical pore size despite the highly interconnected nature of the pore spaces. This procedure was applied to the CAD files (.STL) as well as to the micro-CT scan data for direct comparison. The .STL files were, therefore, voxelized using the same voxel size as the scans, creating synthetic micro-CT data using the function "create volume from mesh". The actual specimen (actual micro-CT data) could, therefore, be aligned to the CAD design using the best-fit alignment registration tool, which was done for all the analyses performed. To compare the overall design with the actual part, the nominal-actual comparison tool was used to obtain a statistical representation of the deviations at each location on the surface of the part. Additional high-resolution scans of the internal sections of the specimens were performed to better visualize the observed strut porosity. This was done at 10 µm voxel size, 100 kV, and 100 µA using a 0.5 mm copper filter. The quantification of the total porosity in the struts was performed in volume fraction values, and visualization in 3D images was done for a number of selected regions. Local porosity color coding was performed, highlighting the location of pore spaces.

2.3. Mechanical testing

The *quasi-static* mechanical properties of the auxetic meta-biomaterials were obtained using a mechanical testing machine (Zwick GmbH & Co. KG, Ulm, Germany) with a 250 kN load cell and a 0.5% crosshead accuracy. A tool steel plate, on either side of the specimens, prevented the machine platens from wearing. The specimens were preloaded (5 N) followed by axial compression for 15 mm with a deformation rate of 2 mm/min. The resulting stress-strain curves were corrected for machine compliance, according to the 'direct technique' [28] and were used to obtain the mechanical properties in accordance with ISO 13,314:2011 [29]. The *quasi-elastic gradient* was calculated in the linear region at the beginning of the stress-strain curve and will from now on be referred to as the elastic modulus. The linear region is generally followed by the first local maximum of the stress-strain curve, corresponding to the *first maximum compressive strength* (FMCS). Due to the ductile behavior of CP-Ti, however, no such maximum was registered. The yield strength (σ_y), which is referred to as the *compressive offset stress*, was measured at 0.2% plastic compressive strain. A previous study on Ti-6Al-4V lattices assumed that the plateau stress was close to the concept of yield strength [20], but significant differences were found in a study on CP-Ti lattices [17]. The plateau stress (σ_p) was, therefore, calculated, as well as the arithmetical mean of the stresses between 20% and 30% compressive strains.

The protocols established in our previous studies regarding the mechanical behavior of bone-mimicking meta-biomaterials were used to perform the fatigue tests [17,20–22]. The specimens were tested on their compression-compression fatigue performance (MTS, Eden-Prairie, USA) using a load ratio (R) of 0.1 and a frequency of 15 Hz (sinusoidal waveform) (Fig. 1). For each type of auxetic meta-biomaterial, the fatigue tests were at least repeated at five different stress levels, resulting in fatigue lives in the range of 10^4 – 10^6 cycles. Two specimens of each de-

Table 2
The morphological properties of the four different auxetic meta-biomaterials, designs A, B, C and D. The SEM data has been presented as mean ± standard deviation, while the mode has been presented for the data acquired using micro-CT.

Type	RD [%]			Strut thickness [mm]			Pore size [mm]	
	CAD	Dry weighing	Micro-CT	CAD	Micro-CT	SEM	CAD	Micro-CT
A	4.6	7.49 ± 0.13	6.3	0.346	0.354	0.402 ± 0.02	2.800	2.653
	24.1	26.01 ± 0.26	25.3	0.871	0.838	0.884 ± 0.04	2.302	2.182
	42.7	42.23 ± 0.37	43.8	1.209	1.190	1.181 ± 0.02	1.930	1.810
B	5.4	8.46 ± 0.14	7.9	0.362	0.364	0.392 ± 0.03	2.620	2.522
	25.4	28.27 ± 0.22	27.0	0.832	0.789	0.837 ± 0.03	2.144	2.065
	45.4	44.04 ± 0.46	46.5	1.163	1.101	1.211 ± 0.04	1.818	1.673
C	4.9	9.32 ± 0.15	8.6	0.261	0.309	0.379 ± 0.03	1.943	1.880
	24.6	26.73 ± 0.19	27.1	0.628	0.592	0.647 ± 0.05	1.585	1.568
	43.2	42.06 ± 0.36	45.4	0.894	0.834	0.873 ± 0.03	1.317	1.322
D	3.4	7.15 ± 0.12	6.7	0.236	0.283	0.371 ± 0.03	2.312	2.165
	17.5	20.10 ± 0.18	19.5	0.580	0.548	0.601 ± 0.04	1.972	1.894
	32.5	32.45 ± 0.24	34.6	0.823	0.777	0.827 ± 0.04	1.730	1.657

sign type were tested for each stress level. A third specimen was tested if the difference in the cycles to failure of these two specimens was more than 40% of their average. Stress and strain values could be calculated using the load and displacement values. Failure was considered to have occurred when the strain (ratcheting) rate showed a rapid increase, matching the abrupt strain jump in the strain *vs.* cycles graph. The slope of the graph ($d\varepsilon/dN$) was, therefore, calculated and the first local maximum was found to correspond to the point of failure. In most cases, this also corresponded with the specimens losing 90% of their stiffness. The machine was stopped once the specimens reached 10^6 loading cycles (run-out specimens). With the fatigue life values and the maximum applied stress, the S-N curves could be obtained. The maximum applied stress values were divided by the respective yield strength, σ_y, and plateau stress, σ_p, to obtain the normalized S-N curves.

2.4. Statistical analysis

Quantitative measurements were expressed as mean ± standard deviation (SD). A first order power law (ax^b) was fitted to the data points of each respective *quasi-static* mechanical property. A similar power law was fitted to the fatigue data points normalized by the yield strength (excl. run-out specimens), either for all or for separate relative density values, depending on the coefficient of determination. This power law was then used to determine the maximum design stress at 10^4 and 10^6 cycles.

3. Results

3.1. Morphological characteristics

The architecture of the AM specimens generally matched their design, with no major unexpected features (Table 1). All struts were built successfully, and limited warping was observed. The higher density specimens that did show signs of warping were processed as described above. While the dimensions of the majority of the specimens lie within 0.10 mm of the intended design, this deviation increased with the relative density as well as with the aspect ratio. The biggest cumulated deviation was found for design C (RD = 0.422) in which 90% of the part was found to lie within 0.17 mm of the CAD design (Table 1). The actual values of the relative density as measured by dry weighing and micro-CT imaging, ranged between 6.3 and 46.5% (Table 2). In all cases, the relative density values were higher than the designed values, with deviations increasing with the aspect ratio and re-entrant angle. A high repeatability in the overall relative density (< 2%) was achieved, with the biggest variations measured in the lower-density specimens. The strut thickness values ranged between 0.28 and 1.21 mm, while the mean pore size was found to vary between 1.32 and 2.65 mm (Table 2). In general, the strut thickness of the lower-density specimens increased as compared to their CAD designs, while the struts of the higher-density specimens lost some of their thickness. In general, the pore size values were smaller than the designed values.

Some microstructural imperfections were found on the surface as well as in the interior of the struts (Fig. 2). Superficial pores were found on the surface of the higher density specimens (Fig. 2A) and a clear difference in surface roughness was observed between downward- and upward-facing surfaces with respect to the build plate (Fig. 2B). Adhering powder particles were primarily present on supported surfaces facing the build plate (Fig. 2B). The local strut porosity was visualized using micro-CT (Fig. 2C-D), showing areas of high porosity surrounded by a more solid shell. Design A (RD = 0.422) was found to have an average internal porosity of 20.3% in the volume fraction that was considered, whereas design D (RD = 0.325) shows a thicker shell with an average porosity of 12.3%. Lower density specimens, like design A (RD = 0.075), were less affected by these imperfections (Fig. 2C-D).

3.2. Quasi-static mechanical properties

While most porous biomaterials show a typical stress-strain curve, including the initial linear region, plateau phase and final densification, these phases are not always as apparent in this type of auxetic meta-biomaterial [14,30]. The lower density specimens (Fig. 3A) exhibited the typical linear region, followed by a plateau phase with a high frequency of fluctuations. The amplitude of the fluctuations decreased with the relative density, almost disappearing in designs A and B (Fig. 3B). The final densification phase, showing a steep increase in the stress, was visible at a relative density of ~0.270 for designs A and B. Increasing the relative density advanced the onset of this final stage, which was also visible for design C (for a relative density of 0.420) (Fig. 3B-C).

All mechanical properties were found to increase with relative density (Fig. 3D-F). The elastic modulus of the auxetic meta-biomaterials was found to vary between 66.31 ± 1.92 MPa and 5648 ± 1433 MPa for relative density values ranging between 0.07 and 0.43 (Fig. 3D). The yield strength of the auxetic meta-biomaterials varied between 1.4 ± 0.04 MPa and 46.70 ± 0.62 MPa for the aforementioned range of relative density (Fig. 3E). The stiffness and strength of the structures were found to increase with the

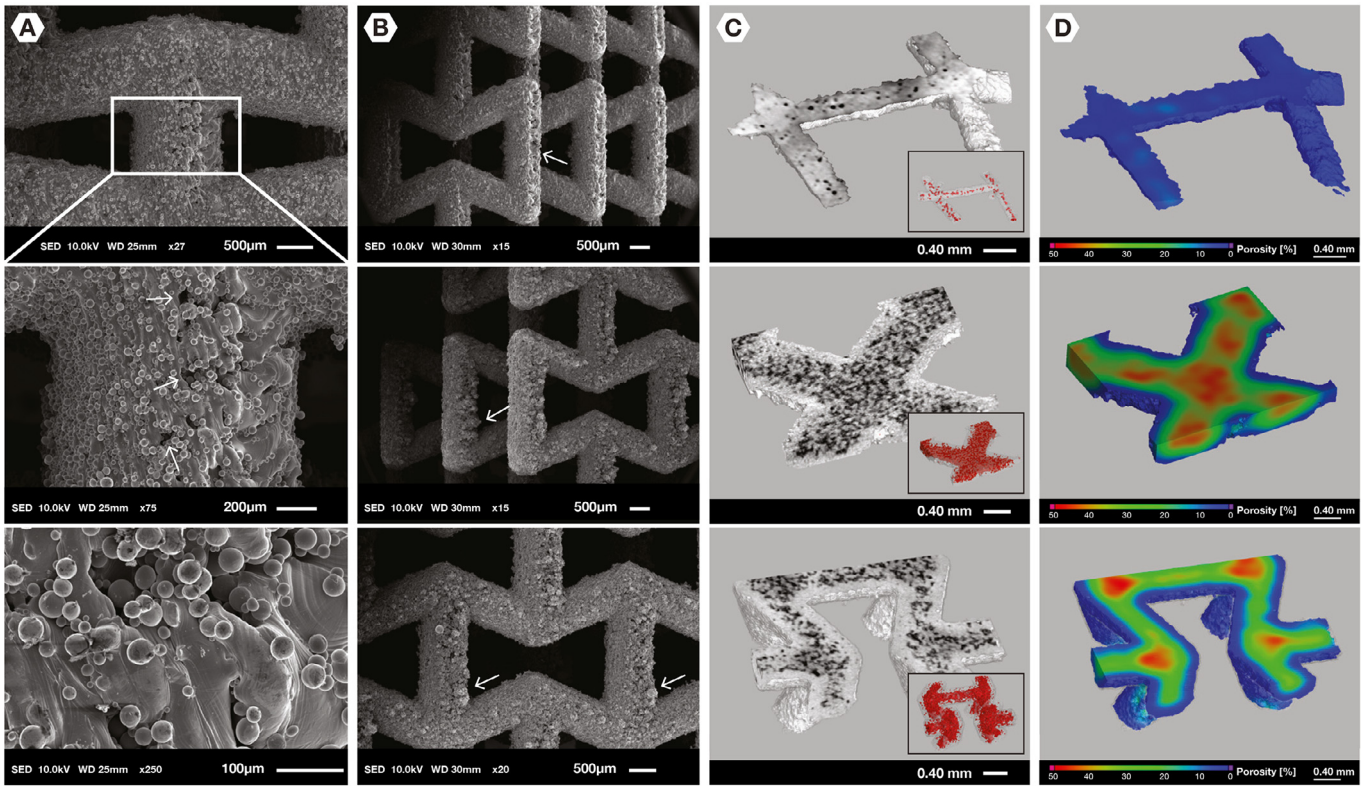

Fig. 2. (A) The structure and surface of design A (RD = 0.422) observed using SEM (27x, 75x, and 250x). (B) The structure and surface of design D (RD = 0.325) observed using SEM at 15x and 20x. (C) The inside morphology of, from top to bottom, design A (RD = 0.075), design A (RD = 0.422), and design D (RD = 0.325) imaged using micro-CT. (D) The local average porosity of, from top to bottom, design A (RD = 0.075), design A (RD = 0.422), and design D (RD = 0.325) imaged using micro-CT.

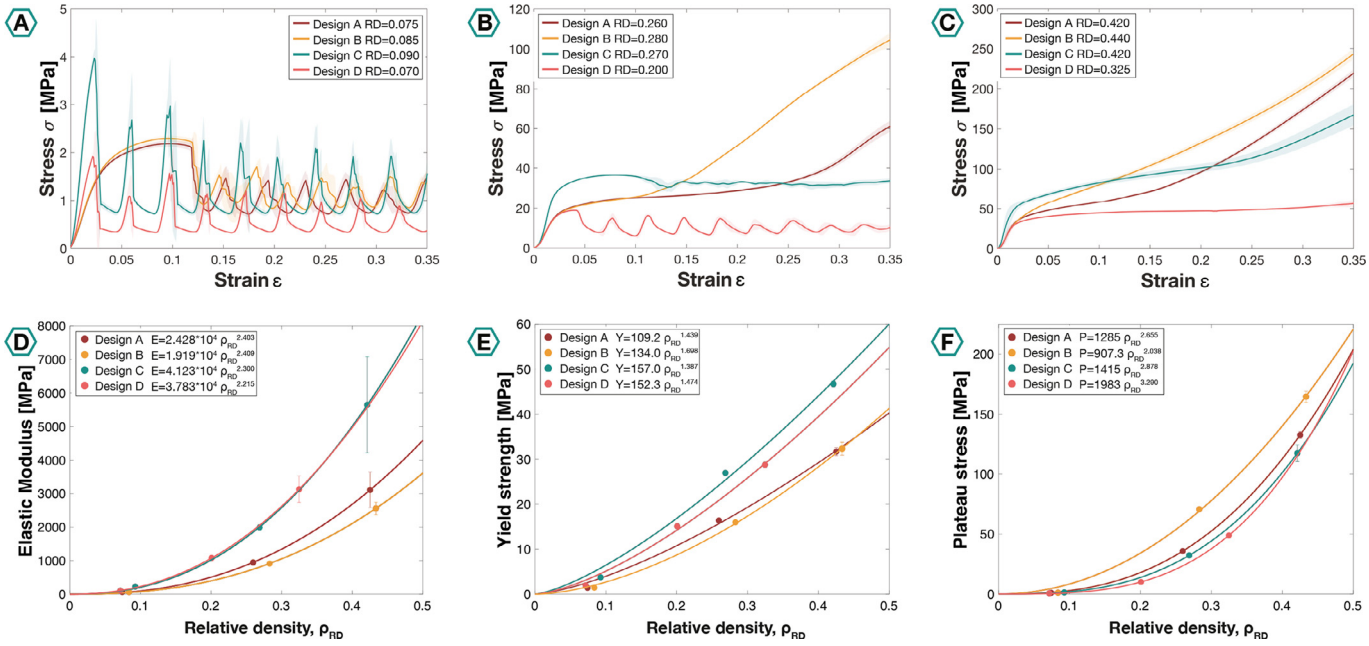

Fig. 3. The stress-strain curves of the auxetic meta-biomaterials with (A) ~5% relative density, (B) ~25% relative density, (C) ~45% relative density, and their derived mechanical properties; (D) elastic modulus, (E) yield strength, and (F) plateau stress together with their fitted power laws.

aspect ratio and decrease with the re-entrant angle, with the highest values found for design C and the lowest for design B. With values ranging between 0.65 ± 0.03 MPa and 164.60 ± 4.66 MPa, the plateau stress was found to decrease with aspect ratio and increase with re-entrant angle. However, some of these relations only seem to become apparent for higher values of the relative density.

3.3. Fatigue behavior

The results of the compression-compression fatigue tests are presented as S-N curves, both for absolute (Fig. 4A) and normalized stress values (Fig. 5). Some of the strain *vs.* cycles graphs have been presented in Fig. 4B, showing the typical three-stage fatigue

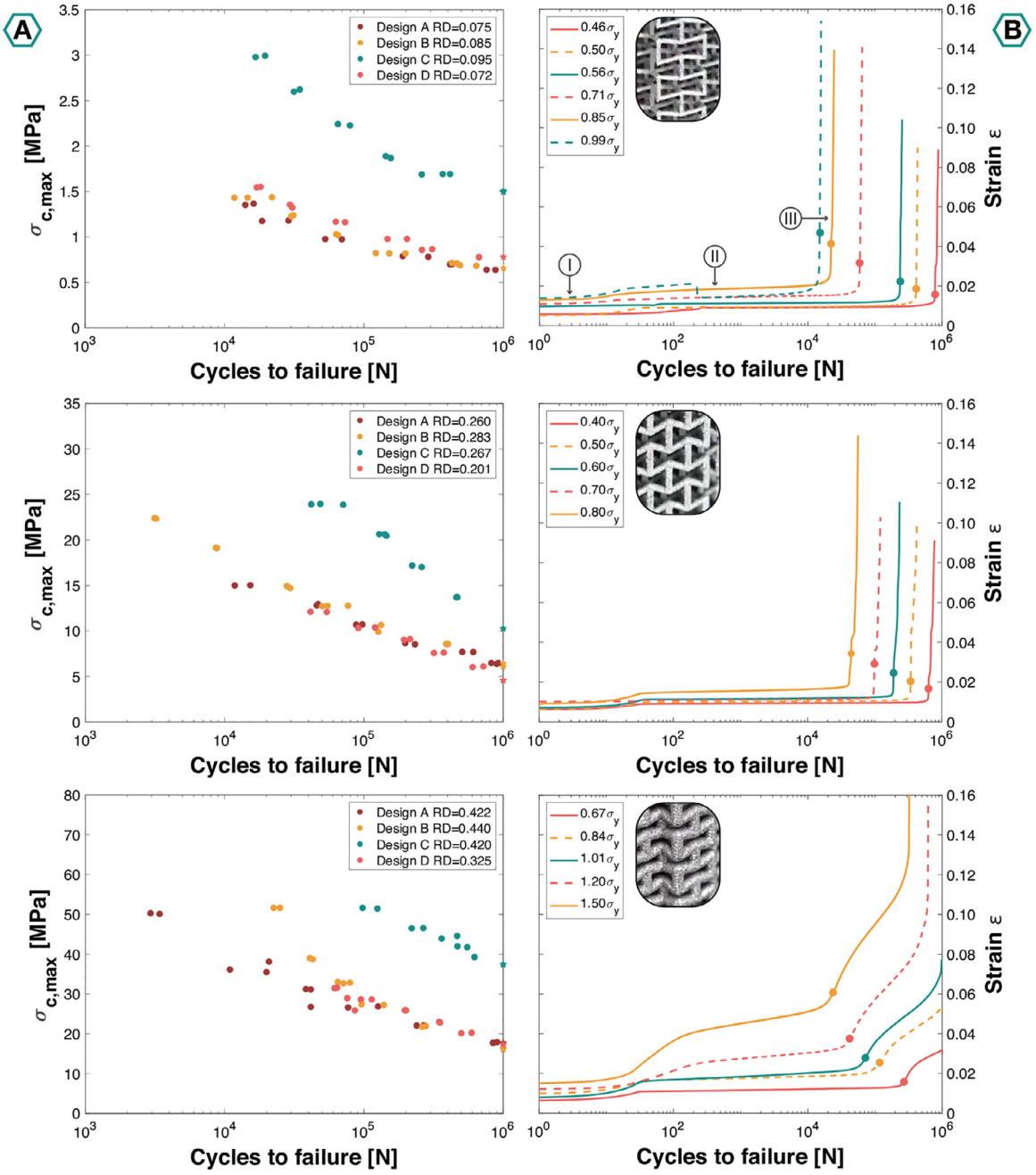

Fig. 4. (A) The absolute S-N curves of all the specimens (grouped per relative density class). The test run-out specimens have been noted by stars. (B) A representative strain *vs.* cycles curve for each relative density class, from top to bottom, design A (RD = 0.075), design D (RD = 0.201), and design B (RD = 0.440). The three-stage fatigue behavior has been indicated by I, II, and III, and the failure points have been noted by circles.

behavior of porous metals [31]. In the first stage (I), the strain slowly increased until reaching the second stage (II) at ~10^2 cycles, in which there is hardly any build-up of strain. In the third stage (III), the strain accumulates very rapidly, exhibiting the highest derivative of strain and the specimen finally fails. Atypical fatigue behavior was observed for some of the higher-density designs, including design A (RD = 0.422) and design B (RD = 0.283, 0.440) (Fig. 4B, bottom). These specimens exhibited multiple strain jumps. Based on the strain *vs.* cycles graphs and visual inspection of the specimens, failure was assumed at the first local maximum of $d\varepsilon/dN$ after stage II (circles, Fig. 4B). The fatigue lives increased by decreasing the applied stress level. The order of the absolute S-N curves matched the order of the yield stress values with the relative density (Figs. 3E and 4A). For designs A and B, a first order power law could be fitted to the S-N datapoints normalized with respect to the yield strength. With a fairly high coefficient of determination, R^2=0.888, the specimens of design A exhibited a maximum design stress of 0.429 σ_y at 10^6 cycles (Fig. 5A). The high relative density specimens of design B (RD = 0.440) started to deviate from the collective power law, resulting in a coefficient of determination of R^2=0.663 and a maximum design stress of 0.501 σ_y at 10^6 cycles. No power law could be fitted to the S-N data points of designs C and D. An average maximum design stress of 0.47 σ_y was found at 10^6 loading cycles. The individual power law for each of the data series (corresponding to the twelve designs) are presented in Table 3, with very high coefficients of determination. Differences were especially visible at 10^4 cycles, but at 10^6 cycles the higher density specimens (~0.45 RD) of designs C and D with-

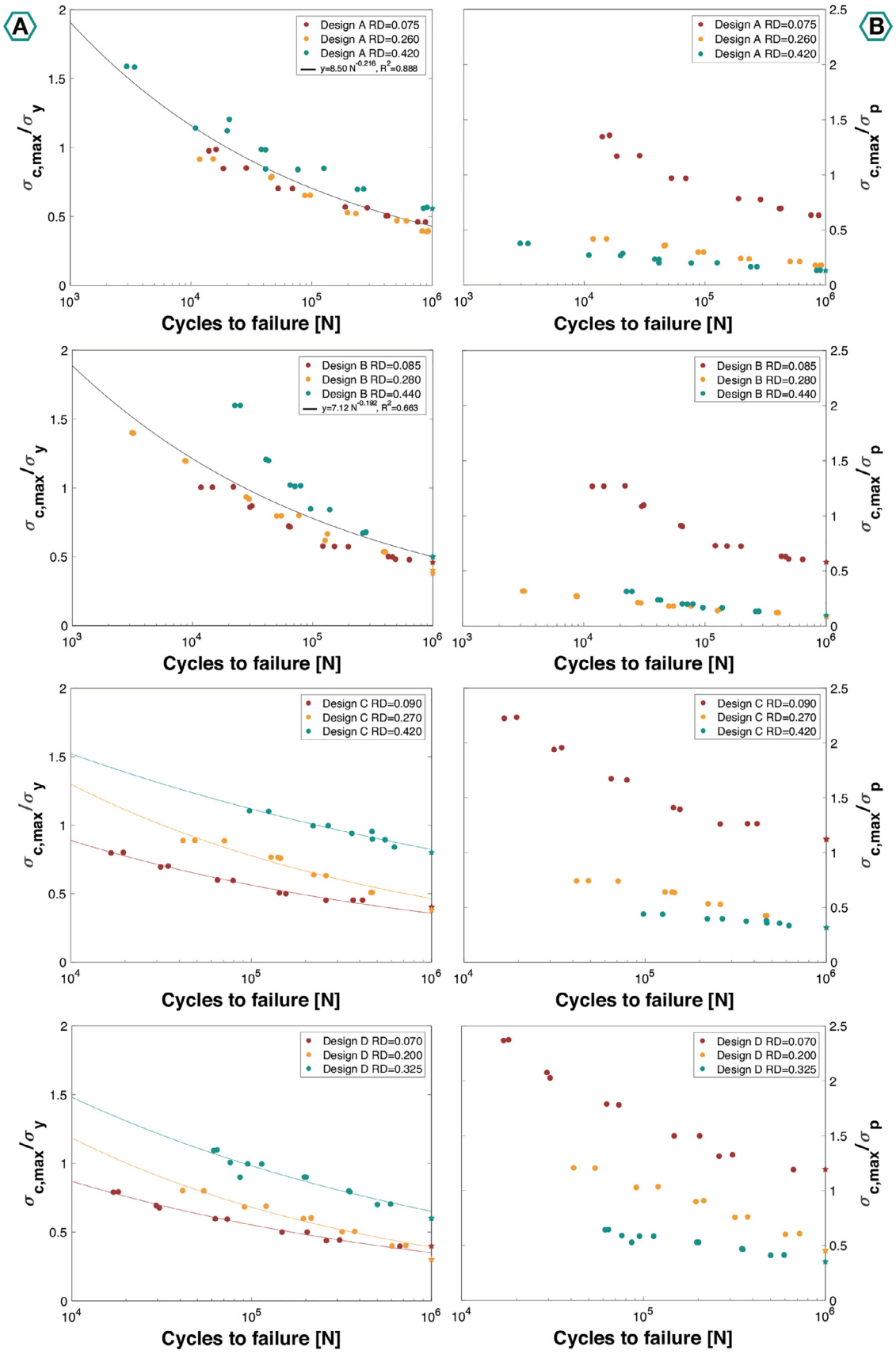

Fig. 5. The S-N curves of all the specimens normalized with respect to their (A) yield and (B) plateau stresses. A first order power law could be fitted in (A) to all the datapoints of design A and B. The run-out specimens have been noted by stars.

Table 3
The power laws fitted to the normalized S-N curves for all the auxetic meta-biomaterials studied here.

Type	RD	Fitted power law	R^2 value	Stress level		Fatigue strength [MPa]
				at 10^4 cycles	at 10^6 cycles	at 10^6 cycles
A	0.075	$5.74 \cdot N^{-0.188}$	0.98	1.020 σ_y	0.430 σ_y	0.596
	0.260	$6.09 \cdot N^{-0.196}$	0.98	0.998 σ_y	0.404 σ_y	6.615
	0.422	$6.96 \cdot N^{-0.185}$	0.97	1.210 σ_y	0.516 σ_y	16.317
B	0.085	$7.70 \cdot N^{-0.213}$	0.97	1.087 σ_y	0.409 σ_y	0.582
	0.283	$7.19 \cdot N^{-0.201}$	0.99	1.131 σ_y	0.448 σ_y	7.163
	0.440	$65.46 \cdot N^{-0.372}$	0.97	2.136 σ_y	0.386 σ_y	12.466
C	0.095	$5.51 \cdot N^{-0.198}$	0.98	0.889σ_y	0.357σ_y	1.333
	0.267	$10.16 \cdot N^{-0.223}$	0.92	1.299σ_y	0.465 σ_y	12.510
	0.420	$5.21 \cdot N^{-0.134}$	0.94	1.522 σ_y	0.823 σ_y	38.423
D	0.072	$5.34 \cdot N^{-0.197}$	0.99	0.870 σ_y	0.351 σ_y	0.687
	0.201	$10.76 \cdot N^{-0.240}$	0.96	1.181 σ_y	0.391 σ_y	5.903
	0.325	$7.65 \cdot N^{-0.178}$	0.91	1.480 σ_y	0.651 σ_y	18.732

stood significantly higher normalized stress values (Fig. 5A). An increase in the aspect ratio decreased the normalized stress within the low cycle regime, while significantly increasing the stress for high cycle fatigue. Considering the latter, an increase in the re-entrant angle decreased the maximum design stress. When normalized with respect to the plateau stress, the S-N curves showed significantly higher values for the lower density specimens of all designs (Fig. 5B). The differences were small for the higher values of the relative density but become more apparent in designs C and D.

The photographs that were taken after fatigue failure show that the struts in the lower density specimens primarily deform by bending, leading to a layer-by-layer collapse (Fig. 6A-B). Increasing the relative density changes the deformation mechanism towards densification and shear. Designs A and B were found to deform and fail completely through all their layers (Fig. 6A), while designs C and D showed a more isolated collapse of layers (Fig. 6B). The hinging of the inverted struts in designs A and B resulted in them touching the inverted struts on the opposite side. The SEM images taken after failure showed a significant internal porosity in the higher-density specimens, with clear fatigue striations and cracks initiating from the void spaces (Fig. 6C). Failure was primarily found to occur at the strut junctions, in relatively straight lines (Fig. 6D). The highest values of the internal porosity were generally found in the struts built close to the horizontal (at 10° with respect to the build plate).

4. Discussion

In this study, four different types of auxetic meta-biomaterials (each of which with three different values of the relative density) were designed and additively manufactured. From previous studies, we know that the *quasi-static* mechanical properties of these designs are vastly different, given the difference in their geometries [6,14]. The fatigue performance of such materials, on the other hand, had never been experimentally explored. The results of this study, therefore, form a promising basis for the application of auxetics in dynamically loaded settings.

4.1. Morphological properties

The relative densities of the auxetic meta-biomaterials were assessed using both dry weighing and micro-CT imaging. In general, both methods showed an increase in the relative density as compared to the CAD designs, with deviations increasing with the relative density, aspect ratio, and re-entrant angle. The same trends were found in a previous study on Ti-6Al-4V auxetic meta-biomaterials, using the same CAD files [14]. The relative density values of design D did not meet the aforementioned classes of ~0.05, ~0.25, and ~0.45 RD. This can be explained by a fault in the design software, resulting in a misinterpretation of the designed density values. The geometry of the re-entrant hexagonal honeycomb pushes the boundaries of the laser powder bed fusion process. The specimens were printed at an angle and this influences the print quality and, thus, the mechanical properties of the structure as a whole [32–34]. Vertical struts generally have a much higher quality than horizontal struts, whereas diagonal struts perform somewhere in between [34]. Due to the oblique build orientation, the vertical struts were now printed at a 10-degree angle, close to the horizontal. Additionally, the staircase effect tends to increase the surface roughness, especially on down-facing surfaces [35], and blob formations may occur in the places where the laser is forced to make acute turns [32,33,36]. Due to these imperfections, the as-manufactured specimens may deviate from their respective CAD files. Additionally, these irregularities can create stress concentrations that are detrimental for the fatigue performance [37,38]. Chemical and (thermo)mechanical surface treatments can be used to improve the fatigue strength, by reducing the surface roughness and removing the potential crack nucleation sites [38–41].

The micro-CT and SEM images revealed that the struts of the higher-density specimens contained areas with significant internal porosity and a large volume of interconnected pore spaces. This micro-porosity, including the size and location of these pores, has been shown to strongly affect the fatigue performance of metallic lattices [42,43]. The SEM images revealed that cracks often originate from these void spaces, although it is unclear whether they were the most deleterious defects [42,44]. Surface defects are as important in determining the fatigue life of these specimens and can more easily be avoided by improving the processing parameters and (post-)AM conditions. The current quality of the auxetic meta-biomaterials is a direct result of the chosen printing parameters, in which a trade-off was made to obtain a good quality structure while achieving a reasonable build rate. Further optimization and validation of the scanning parameters could, therefore, lead to decreased internal porosity, thereby improving the fatigue performance of auxetic meta-biomaterials.

4.2. Static mechanical performance

The stress-strain curves of the auxetic meta-biomaterials tested here showed that there are clear differences in the deformation behaviors of various auxetic designs, especially for the smaller values of relative density. Due to the ductility of CP-Ti, the structures continuously deform under the applied compressive load. With a high slenderness ratio, the struts do eventually fail, resulting in a layer-by-layer collapse. The strain at failure of designs A and B was, however, much higher than those of designs C and D. For the higher

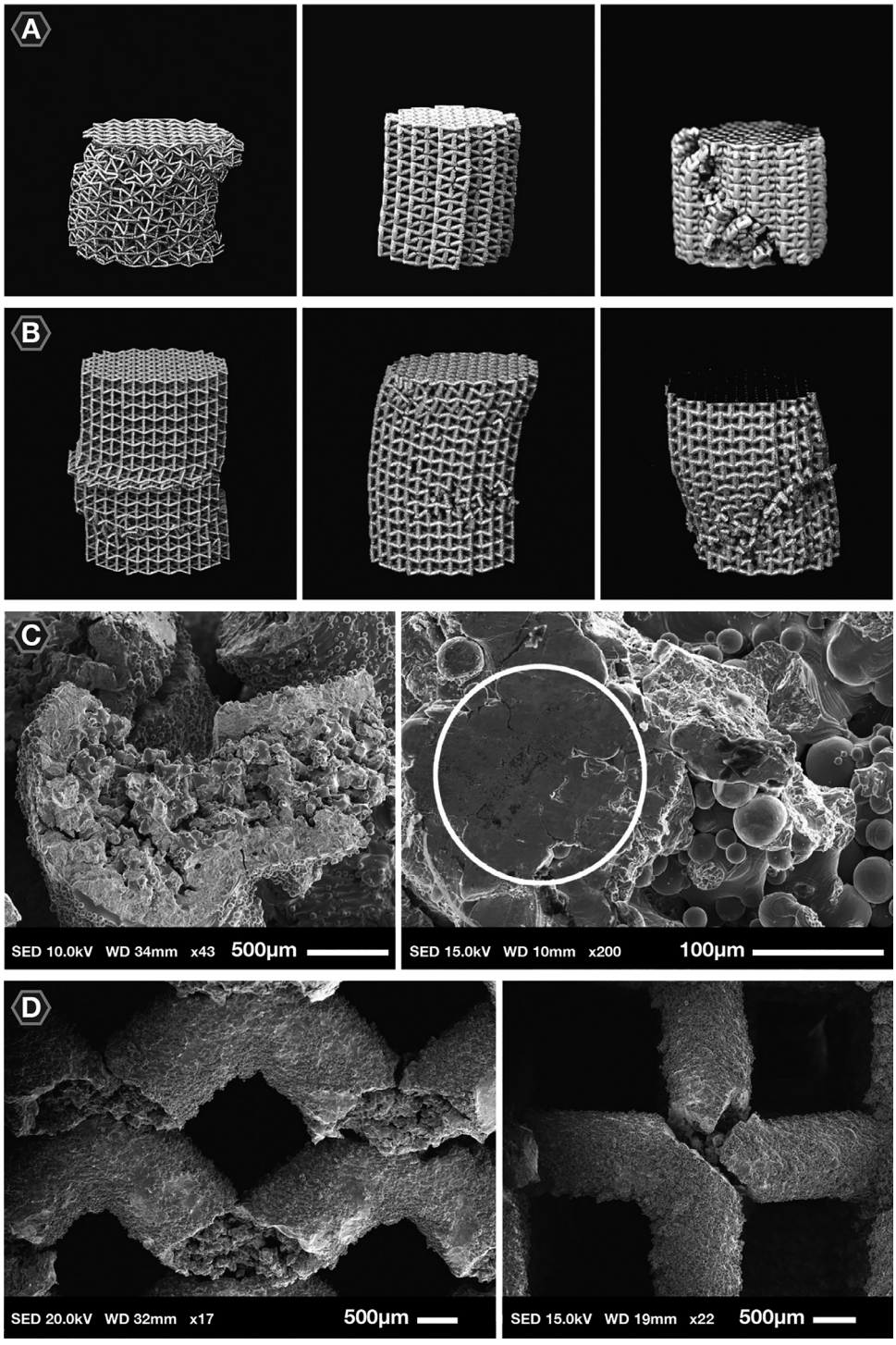

Fig. 6. The appearance of the specimens after fatigue testing. The deformation after failure of (A) design A (RD = 0.075, 0.260, and 0.422), and (B) design C (RD = 0.095, 0.267, and 0.420). (C) The SEM images showing the internal strut porosity and crack initiation from the voids. (D) The occurrence of macro-cracks at the struts junctions.

values of the relative density, the structures do not reach a first local maximum, similar to the results reported by Wauthle et al. (2015) and a previous study of ours on Ti-6Al-4V auxetic meta-biomaterials [14,17]. According to Gibson and Ashby (1999), these cellular solids go through early densification [45]. With a small aspect ratio and thicker struts, the cell walls touch at lower values of strain (designs A and B). In this study, the ductility of the bulk material enhances that effect. This could also explain the delayed failure of designs A and B for the lower values of relative density, in which strain accumulates while the stress remains nearly constant. The geometry-property relationships that were found regarding the mechanical properties are in line with the relationships found in earlier studies [6,14].

The mechanical properties of meta-biomaterials depend on their small-scale architecture, hence their dependence on the type of unit cell. Significant differences have been found between

stretch- and bending-dominated unit cells [14,46–48]. As compared to stretch-dominated unit cells (*e.g.*, cube and truncated cuboctahedron), the re-entrant hexagonal honeycomb is very compliant. As a bending-dominated unit cell, its stiffness is comparable to unit cells such as the diamond, body-centered cubic, and rhombic dodecahedron [46,47]. In contrast to the auxetic meta-biomaterials studied here, these unit cells have a positive Poisson's ratio. Combining both positive and negative Poisson's ratio has been shown to be beneficial in the design of a hip stem, fighting the longstanding problem of implant loosening [5]. However, the theoretical upper bound defining the maximum elastic modulus of architected materials (Hashin–Shtrikman bounds) [49] is lower for auxetic materials and decreases as the Poisson's ratio further decreases. The lower *quasi-static* mechanical properties of auxetic meta-biomaterials as compared to those of non-auxetic meta-biomaterials is, however, not necessarily a major problem. The bulk properties of metallic biomaterials generally exceed those of the bone by a few orders of magnitude. The challenge, therefore, usually lies in decreasing those properties to the level of the bony tissue. Using a higher value of the relative density is generally all that is needed to increase the mechanical properties of auxetic meta-biomaterials.

4.3. Fatigue behavior

Before auxetic meta-biomaterials can be adopted in the field of orthopedics, their fatigue behavior needs to be fully understood. All structures exhibited the typical three-stage fatigue behavior found in porous metals [31]. However, the strain *vs.* cycles graphs revealed multiple strain jumps for some of the designs (Fig. 4B), including a very high initial displacement. Unlike many other fatigue studies, we could, therefore, not define the failure point using a 90% stiffness drop [17,20,21]. These strain jumps were also found in the compression fatigue testing of aluminum foams, pointing at the formation of cyclic deformation bands [31]. According to Yavari et al. (2013), AM porous structures show a more uniform plastic deformation as compared to porous structures manufactured using conventional techniques [20]. Other studies on AM porous structures therefore did not observe these strain jumps [20,50]. This also holds true for most of our structures (Fig. 4B, 6B), but designs A and B were different. The multiple strain jumps and 'plateau' phases point at several layers of densification. This could be explained by the relatively small space in between their inclined struts as compared to designs C and D. Upon deformation, these struts touch each other, causing the structure to densify. Once the densification strain has been reached, the structure will experience another strain jump through the collapse of another layer. Additionally, these structures entered the third stage over a range of strain values (~0.02–0.06, Fig. 4B) depending on the applied stress level. The same phenomenon has been observed in aluminum foams, but not for the first strain jump [31].

The absolute maximum design stress at 10^6 loading cycles is comparable for the designs with a similar aspect ratio, indicating that the differences in the re-entrant angles of the various auxetic structures considered here do not significantly influence the fatigue performance (Fig. 4A). There is, however, a difference between designs C and D, which is likely caused by their difference in relative density. The highest absolute maximum design stress was found for design C, which is in line with its higher strength and stiffness. The observations regarding the normalized stress levels were, however, more remarkable (Fig. 5). A collective power law could be fitted to the data points of designs A and B, but the higher-density structures of design C and D did not line up. As a consequence of this difference, the S-N curves do not collapse to one single curve after normalization, unlike many other unit cells [17,20,21]. It is therefore very difficult to predict the fatigue performance of the auxetic meta-biomaterials based on the re-entrant hexagonal honeycomb unit cell. In this case, we also observed significant differences between the normalized design maxima at higher values of relative density. This may have been caused by the different angles of the oblique struts. AM meta-biomaterials generally deform because of both bending and buckling, and their fatigue behavior is often determined by the interaction of cyclic ratcheting and fatigue crack growth [50,51]. The re-entrant hexagonal honeycomb is a bending-dominated unit cell and the inclined struts therefore experience both tension and compression [6,14]. Compressive forces generally cause crack closure and may slow down crack growth, whereas tensile forces are most likely to cause fatigue failure [18,21,52]. The accumulation of plastic deformation upon cyclic loading (ratcheting) can be decreased by increasing the compressive stress in the struts [21,50,53]. In our designs, this was achieved by increasing the re-entrant angle, which led to the increasing fatigue performance from design A to design D (Fig. 5A). It should be noted that designs A and B do perform better within the low cycle fatigue regime ($<10^4$ cycles). Furthermore, a relatively high percentage of void space was found in the struts of designs A and B. This does, however, not explain the differences in normalized design maxima between the different relative densities of the same design. Li et al. (2012) showed that the cyclic ratcheting rate is sensitive to the relative density, but this merely explains the higher fatigue lives found in the higher-density structures [51]. In an earlier study, we found that the negative Poisson's ratio of these auxetic meta-biomaterials decreases as the relative density increases, as a direct result of the thickened strut junctions [14]. The bending of the struts will, therefore, become more difficult and buckling will become the primary deformation mode. As a result, the struts in designs C and D will primarily experience compressive forces, which further increase with the relative density and extend their fatigue life. The relatively small re-entrant angle in designs A and B, and the early densification caused by strut contact, may be the reason for the absence of this phenomenon.

When compared to non-auxetic meta-biomaterials made from CP-Ti, the auxetic meta-biomaterials studied here tend to exhibit an improved fatigue performance. Zhao et al. (2018) presented the maximum stress levels of tetrahedron and octahedron meta-biomaterials, which ranged between 0.32 σ_y and 0.57 $\sigma_y\sigma_y$ at 10^6 loading cycles [54]. A normalized design maximum of 0.41 $\sigma_y\sigma_y$ was reported in the study of Wauthle et al. (2015) for dodecahedron-based structures, which approaches our average (0.47 $\sigma_y\sigma_y$). Despite their great static resemblance with rhombic dodecahedron structures, the auxetic meta-biomaterials exhibit a significantly higher maximum design stress [53]. Just like our specimens, the specimens based on the rhombic dodecahedron unit cell exhibited fatigue cracks in the vicinity of their strut junctions [53]. The extraordinary maxima observed here even surpass the limit of a topology-optimized structure that was designed for optimal fatigue performance [53]. The absolute applied stress levels are, on the other hand, quite low and therefore easily surpassed by stretch-dominated meta-biomaterials, such as the tetra- and octahedron [54]. This is a direct consequence of the lower elastic modulus of auxetic structures, as discussed above within the context of the Hashin–Shtrikman bounds. Altogether, our observations support the fact that auxetic structures exhibit superior normalized fatigue strength as compared to other non-auxetic geometries [9,11].

4.4. Bone-mimicking requirements in biomedical implants

The values found in the literature regarding the most optimal morphological properties for bone tissue regeneration are quite diverse, partly because *in-vitro* and *in-vivo* optima greatly differ [55–57]. A higher porosity is said to enhance osteogenesis [55,57],

but it also decreases the mechanical strength and integrity of the structure. As a consequence, the morphological and mechanical properties should be simultaneously optimized for functionality and biological effectiveness. Given their relative density values (<0.50 RD), the structures in this study are expected to support the formation of *de novo* bone tissue [58]. In terms of the pore size, bigger pores (>1000 μm) would favor direct osteogenesis, as they prevent the pores from being occluded and facilitate cell growth through the optimal transport of oxygen and nutrients [55,59,60]. Smaller pores (100–300 μm) tend to decrease the permeability, but may increase the cell attachment [61]. A smart meta-biomaterial may, therefore, be functionally graded, providing both smaller pores for initial cell attachment and larger pores for further proliferation and growth [59,60]. The presented mode values are larger than the recommended pore sizes [55,58,61,62], but the statistical representations show that each specimen has multiple pore sizes that do fall within the recommended range. The smaller superficial pores that were found on the surface of the struts, as a direct result of the printing imperfections, may improve bony ingrowth and, thus, implant fixation [55,63–67]. However, they tend to decrease the fatigue performance as well. Surface treatments, such as sand-blasting, chemical etching, and even laser modification could be used to provide a smooth implant surface with sufficient texture for cell attachment, while retaining the desired bulk mechanical properties [38,39,68].

While bone-mimicking meta-biomaterials should provide adequate mechanical support, they should not be too stiff. To prevent stress shielding, the auxetic meta-biomaterials should mimic the mechanical properties of the host bone [69,70]. Bobyn et al. (1992) even hypothesize a 2:1 or 3:1 stiffness ratio (femur to stem) [70]. Considering the increase in stiffness of a porous meta-biomaterial once bone regeneration progresses [71], this seems a plausible approach. Considering the pure titanium used in this study, a relative density of 30–40% would best mimic the mechanical properties of trabecular bone [72]. In this case, the auxetic meta-biomaterials will still have sufficient strength and stiffness to be applied as bone substitutes [73,74].

As a bone substitute, meta-biomaterials generally experience cyclic loading. In this study, we determined the fatigue limit at 10^6 cycles based on an average patient walking activity of 2 million cycles/year and a bone fracture healing time of ~21–24 weeks [75,76]. During this healing time, the bone will start to grow into the implant, thereby significantly increasing the fatigue performance of the bone-implant complex [71]. Until then, the auxetic meta-biomaterial should be able to provide mechanical support. Given the high variety of loading regimes in the human body and the parameters affecting the musculoskeletal loading, it is impossible to define the exact response that an auxetic meta-biomaterial should exhibit in order to function in orthopedic implants. In addition to the above-mentioned factors, the optimal properties of meta-biomaterials may also depend on the patient's anatomy and attributes. Computational models could, therefore, help in determining the patient-specific requirements, which could then be used to design the optimal implant. Empirical relationships or finite element models will, therefore, be needed to predict the deformation and failure of such meta-biomaterials. The data presented here could serve as a means to verify any such model, given the high number of unpredictable imperfections caused by the AM process.

The use of CP-Ti ensured that the structures could continuously deform without failure, in contrast to the widely applied Ti-6Al-4V alloy [14]. A higher ductility influences the ratcheting rate, as the material will be able to withstand a larger amount of plastic strain before cracking [53,77]. This plasticity-driven mechanism decreases the crack initiation and propagation, thereby enhancing the fatigue performance [17,77]. As compared to the more brittle Ti-6Al-4V alloy, the use of CP-Ti may substantially increase the (normalized) maximum design stress of AM porous structures [17,22].

4.5. Future research

Compression is often considered the most dominant loading mode in the musculoskeletal system, hence the numerous studies on compression-compression fatigue testing of meta-biomaterials [17–22]. Our work considered compression as well, both because of its importance as the dominant loading mode and the fact that it enables us to compare the results obtained here with those reported previously on other non-auxetic meta-biomaterials. It is, however, important to study the fatigue behavior of auxetic meta-biomaterials under other loading regimes including tension and bending. In the aforementioned design of a hip stem, the structure is primarily subjected to tensile stresses, which should therefore be the focus of future research [5].

As mentioned before, the biological response to auxetic meta-biomaterials is still unclear. A few studies have investigated the effects of a negative Poisson's ratio on the response of bone cells. The results have, however, been inconclusive [78,79]. Further research is needed to understand how the Poisson's ratio of (auxetic) meta-biomaterials affects the proliferation and differentiation of bone cells.

5. Conclusions

The compression-compression fatigue performance of AM auxetic meta-biomaterials made from CP-Ti was studied. The different parameters defining the geometry of the re-entrant hexagonal honeycomb unit cell, including its aspect ratio, re-entrant angle, and relative density, were varied to create auxetic meta-biomaterials with different geometrical designs. The morphology, static mechanical performance, and fatigue behavior of twelve different designs were assessed. All of the designs conformed well to their intended geometry. Both morphological and static mechanical properties of the resulting specimens were generally appropriate for bone replacement purposes. The S-N curves of the majority of the experimental groups exhibited the typical three-stage fatigue behavior, but a minority exhibited multiple strain jumps, indicating a non-uniform plastic deformation. With an average maximum design stress of 0.47 σ_y at 10^6 cycles (range: 0.35 σ_y-0.82 σ_y), the auxetic meta-biomaterials studied here showed an exceptional fatigue performance. Despite being a bending-dominated architecture, the re-entrant hexagonal honeycomb exhibits maximum design stresses that are closer to some of the stretch-dominated unit cells. With these results, we are one step closer towards the adoption of auxetic meta-biomaterials in load-bearing applications, such as hip stems made from a combination of meta-biomaterials with positive and negative Poisson's ratio values. Further optimization and validation of the scanning parameters and the potential application of post-processing treatments could further improve their fatigue performance.

Declaration of Competing Interest

The authors declare that they have no known competing financial interests or personal relationships that could have appeared to influence the work reported in this paper.

Acknowledgements

The research for this paper was financially supported by the Prosperos project, funded by the Interreg VA Flanders – The Netherlands program, CCI Grant No. 2014TC16RFCB04.

Disclosures

None.

References

[1] S.M. Kurtz, E. Lau, K. Ong, K. Zhao, M. Kelly, K.J. Bozic, Future young patient demand for primary and revision joint replacement: national projections from 2010 to 2030, Clin. Orthop. Relat. Res.® 467 (10) (2009) 2606–2612.

[2] S. Kurtz, K. Ong, E. Lau, F. Mowat, M. Halpern, Projections of primary and revision hip and knee arthroplasty in the United States from 2005 to 2030, Jbjs. 89 (4) (2007) 780–785.

[3] F. Bobbert, K. Lietaert, A.A. Eftekhari, B. Pouran, S. Ahmadi, H. Weinans, A. Zadpoor, Additively manufactured metallic porous biomaterials based on minimal surfaces: a unique combination of topological, mechanical, and mass transport properties, Acta Biomater 53 (2017) 572–584.

[4] A.A. Zadpoor, Mechanical meta-materials, Mater Horiz 3 (5) (2016) 371–381.

[5] H.M. Kolken, S. Janbaz, S.M. Leeflang, K. Lietaert, H.H. Weinans, A.A. Zadpoor, Rationally designed meta-implants: a combination of auxetic and conventional meta-biomaterials, Mater Horiz 5 (1) (2018) 28–35.

[6] H.M. Kolken, A. Zadpoor, Auxetic mechanical metamaterials, RSC Adv 7 (9) (2017) 5111–5129.

[7] J. Wolff, Das gesetz der transformation der knochen, A Hirshwald 1 (1892) 1–152.

[8] M. Benedetti, A. Du Plessis, R. Ritchie, M. Dallago, J. Razavi, F. Berto, Architected cellular materials: a review on their mechanical properties towards fatigue-tolerant design and fabrication, Mater. Sci. Eng.: R 144 (2021) 100606.

[9] V. Lvov, F. Senatov, A. Stepashkin, A. Veveris, M. Pavlov, A. Komissarov, Low–cycle fatigue behavior of 3D-printed metallic auxetic structure, Mater. Today: Proceedings (2020).

[10] E. Khare, S. Temple, I. Tomov, F. Zhang, S.K. Smoukov, Low fatigue dynamic auxetic lattices with 3D printable, multistable, and tuneable unit cells, Frontiers in Materials 5 (2018) 45.

[11] J. Michalski, T. Strek, Fatigue life of auxetic *Re*-entrant honeycomb structure, in: International Scientific-Technical Conference MANUFACTURING, Springer, 2019, pp. 50–60.

[12] A. Bezazi, F. Scarpa, Mechanical behaviour of conventional and negative Poisson's ratio thermoplastic polyurethane foams under compressive cyclic loading, Int J Fatigue 29 (5) (2007) 922–930.

[13] F. Scarpa, L. Ciffo, J. Yates, Dynamic properties of high structural integrity auxetic open cell foam, Smart Mater. Struct. 13 (1) (2003) 49.

[14] H. Kolken, K. Lietaert, T. van der Sloten, B. Pouran, A. Meynen, G. Van Loock, H. Weinans, L. Scheys, A.A. Zadpoor, Mechanical performance of auxetic meta-biomaterials, J Mech Behav Biomed Mater 104 (2020) 103658.

[15] J.A. Helsen, Y. Missirlis, Biomaterials: a Tantalus Experience, Springer Science & Business Media, 2010.

[16] M. Niinomi, Biologically and mechanically biocompatible titanium alloys, Mater. trans. 49 (10) (2008) 2170–2178.

[17] R. Wauthle, S.M. Ahmadi, S.A. Yavari, M. Mulier, A.A. Zadpoor, H. Weinans, J. Van Humbeeck, J.-.P. Kruth, J. Schrooten, Revival of pure titanium for dynamically loaded porous implants using additive manufacturing, Mater. Sci. Eng.: C 54 (2015) 94–100.

[18] J. de Krijger, C. Rans, B. Van Hooreweder, K. Lietaert, B. Pouran, A.A. Zadpoor, Effects of applied stress ratio on the fatigue behavior of additively manufactured porous biomaterials under compressive loading, J Mech Behav Biomed Mater 70 (2017) 7–16.

[19] A.A. Zadpoor, Mechanical performance of additively manufactured meta-biomaterials, Acta Biomater 85 (2019) 41–59.

[20] S.A. Yavari, R. Wauthlé, J. van der Stok, A. Riemslag, M. Janssen, M. Mulier, J.-.P. Kruth, J. Schrooten, H. Weinans, A.A. Zadpoor, Fatigue behavior of porous biomaterials manufactured using selective laser melting, Mater. Sci. Eng.: C 33 (8) (2013) 4849–4858.

[21] S.A. Yavari, S. Ahmadi, R. Wauthle, B. Pouran, J. Schrooten, H. Weinans, A. Zadpoor, Relationship between unit cell type and porosity and the fatigue behavior of selective laser melted meta-biomaterials, J Mech Behav Biomed Mater 43 (2015) 91–100.

[22] S. Ahmadi, R. Hedayati, Y. Li, K. Lietaert, N. Tümer, A. Fatemi, C. Rans, B. Pouran, H. Weinans, A. Zadpoor, Fatigue performance of additively manufactured meta-biomaterials: the effects of topology and material type, Acta Biomater 65 (2018) 292–304.

[23] R. Hedayati, N. Ghavidelnia, Analytical Relationships For Re-Entrant Honeycombs, 2020.

[24] 3DSystems, Laserform ti gr1 (A), 2017.

[25] A. Du Plessis, I. Yadroitsev, I. Yadroitsava, S.G. Le Roux, X-ray microcomputed tomography in additive manufacturing: a review of the current technology and applications, 3D Printing and Additive Manuf. 5 (3) (2018) 227–247.

[26] T. Hildebrand, P. Rüegsegger, A new method for the model-independent assessment of thickness in three-dimensional images, J Microsc 185 (1) (1997) 67–75.

[27] A. Du Plessis, I. Yadroitsava, I. Yadroitsev, S. le Roux, D. Blaine, Numerical comparison of lattice unit cell designs for medical implants by additive manufacturing, Virtual Phys. Prototyp. 13 (4) (2018) 266–281.

[28] S. Kalidindi, A. Abusafieh, E. El-Danaf, Accurate characterization of machine compliance for simple compression testing, Exp Mech 37 (2) (1997) 210–215.

[29] I. Standard, ISO 13314: 2011 (E) (2011) Mechanical testing of metals—ductility testing—compression test for porous and cellular metals, Ref number ISO 13314(13314) 1-7.

[30] R. Hedayati, S. Ahmadi, K. Lietaert, B. Pouran, Y. Li, H. Weinans, C. Rans, A. Zadpoor, Isolated and modulated effects of topology and material type on the mechanical properties of additively manufactured porous biomaterials, J Mech Behav Biomed Mater 79 (2018) 254–263.

[31] Y. Sugimura, A. Rabiei, A.G. Evans, A. Harte, N.A. Fleck, Compression fatigue of a cellular Al alloy, Mater. Sci. Eng.: A 269 (1–2) (1999) 38–48.

[32] S.L. Sing, F.E. Wiria, W.Y. Yeong, Selective laser melting of lattice structures: a statistical approach to manufacturability and mechanical behavior, Robot Comput Integr Manuf 49 (2018) 170–180.

[33] S. Van Bael, G. Kerckhofs, M. Moesen, G. Pyka, J. Schrooten, J.-.P. Kruth, Micro-CT-based improvement of geometrical and mechanical controllability of selective laser melted Ti6Al4V porous structures, Mater. Sci. Eng.: A 528 (24) (2011) 7423–7431.

[34] R. Wauthle, B. Vrancken, B. Beynaerts, K. Jorissen, J. Schrooten, J.-.P. Kruth, J. Van Humbeeck, Effects of build orientation and heat treatment on the microstructure and mechanical properties of selective laser melted Ti6Al4V lattice structures, Additive Manuf. 5 (2015) 77–84.

[35] J.C. Fox, S.P. Moylan, B.M. Lane, Effect of process parameters on the surface roughness of overhanging structures in laser powder bed fusion additive manufacturing, Procedia Cirp. 45 (2016) 131–134.

[36] T. Craeghs, S. Clijsters, E. Yasa, F. Bechmann, S. Berumen, J.-.P. Kruth, Determination of geometrical factors in layerwise laser melting using optical process monitoring, Opt Lasers Eng 49 (12) (2011) 1440–1446.

[37] J. Pegues, M. Roach, R.S. Williamson, N. Shamsaei, Surface roughness effects on the fatigue strength of additively manufactured Ti-6Al-4V, Int J Fatigue 116 (2018) 543–552.

[38] S. Ahmadi, R. Kumar, E. Borisov, R. Petrov, S. Leeflang, Y. Li, N. Tümer, R. Huizenga, C. Ayas, A. Zadpoor, From microstructural design to surface engineering: a tailored approach for improving fatigue life of additively manufactured meta-biomaterials, Acta Biomater 83 (2019) 153–166.

[39] B. Van Hooreweder, Y. Apers, K. Lietaert, J.-.P. Kruth, Improving the fatigue performance of porous metallic biomaterials produced by Selective Laser Melting, Acta Biomater 47 (2017) 193–202.

[40] E. Maleki, S. Bagherifard, M. Bandini, M. Guagliano, Surface post-treatments for metal additive manufacturing: progress, challenges, and opportunities, Additive Manuf. (2020) 101619.

[41] S. Bagehorn, J. Wehr, H. Maier, Application of mechanical surface finishing processes for roughness reduction and fatigue improvement of additively manufactured Ti-6Al-4V parts, Int J Fatigue 102 (2017) 135–142.

[42] S. Tammas-Williams, P. Withers, I. Todd, P. Prangnell, The influence of porosity on fatigue crack initiation in additively manufactured titanium components, Sci Rep 7 (1) (2017) 1–13.

[43] A. du Plessis, S. Razavi, F. Berto, The effects of microporosity in struts of gyroid lattice structures produced by laser powder bed fusion, Mater Des 194 (2020) 108899.

[44] Y. Murakami, Material defects as the basis of fatigue design, Int J Fatigue 41 (2012) 2–10.

[45] L.J. Gibson, M.F. Ashby, Cellular Solids: Structure and Properties, Cambridge university press, 1999.

[46] C.P. de Jonge, H. Kolken, A.A. Zadpoor, Non-auxetic mechanical metamaterials, Materials (Basel) 12 (4) (2019) 635.

[47] H. Kolken, C. de Jonge, T. van der Sloten, A.F. Garcia, B. Pouran, K. Willemsen, H. Weinans, A. Zadpoor, Additively manufactured space-filling meta-implants, Acta Biomater (2021), doi:10.1016/j.actbio.2021.02.020.

[48] V. Deshpande, M. Ashby, N. Fleck, Foam topology: bending *versus* stretching dominated architectures, Acta Mater 49 (6) (2001) 1035–1040.

[49] I. Ostanin, G. Ovchinnikov, D.C. Tozoni, D. Zorin, A parametric class of composites with a large achievable range of effective elastic properties, J Mech Phys Solids 118 (2018) 204–217.

[50] S. Zhao, S. Li, W. Hou, Y. Hao, R. Yang, R. Misra, The influence of cell morphology on the compressive fatigue behavior of Ti-6Al-4V meshes fabricated by electron beam melting, J Mech Behav Biomed Mater 59 (2016) 251–264.

[51] S. Li, L.E. Murr, X. Cheng, Z. Zhang, Y. Hao, R. Yang, F. Medina, R. Wicker, Compression fatigue behavior of Ti–6Al–4V mesh arrays fabricated by electron beam melting, Acta Mater 60 (3) (2012) 793–802.

[52] J. Schijve, Fatigue of Structures and Materials, Springer Science & Business Media, 2001.

[53] Y. Liu, D. Ren, S. Li, H. Wang, L. Zhang, T. Sercombe, Enhanced fatigue characteristics of a topology-optimized porous titanium structure produced by selective laser melting, Additive Manuf. 32 (2020) 101060.

[54] D. Zhao, Y. Huang, Y. Ao, C. Han, Q. Wang, Y. Li, J. Liu, Q. Wei, Z. Zhang, Effect of pore geometry on the fatigue properties and cell affinity of porous titanium scaffolds fabricated by selective laser melting, J Mech Behav Biomed Mater 88 (2018) 478–487.

[55] V. Karageorgiou, D. Kaplan, Porosity of 3D biomaterial scaffolds and osteogenesis, Biomaterials 26 (27) (2005) 5474–5491.

[56] A.A. Zadpoor, Bone tissue regeneration: the role of scaffold geometry, Biomater Sci 3 (2) (2015) 231–245.

[57] N. Abbasi, S. Hamlet, R.M. Love, N.-.T. Nguyen, Porous scaffolds for bone regeneration, J. Sci. Adv. Mater. Dev. 5 (1) (2020) 1–9.

[58] S. Arabnejad, R.B. Johnston, J.A. Pura, B. Singh, M. Tanzer, D. Pasini, High-strength porous biomaterials for bone replacement: a strategy to assess the interplay between cell morphology, mechanical properties, bone ingrowth and manufacturing constraints, Acta Biomater 30 (2016) 345–356.
[59] S. Van Bael, Y.C. Chai, S. Truscello, M. Moesen, G. Kerckhofs, H. Van Oosterwyck, J.-.P. Kruth, J. Schrooten, The effect of pore geometry on the *in vitro* biological behavior of human periosteum-derived cells seeded on selective laser-melted Ti6Al4V bone scaffolds, Acta Biomater 8 (7) (2012) 2824–2834.
[60] E. Onal, J.E. Frith, M. Jurg, X. Wu, A. Molotnikov, Mechanical properties and *in vitro* behavior of additively manufactured and functionally graded Ti6Al4V porous scaffolds, Metals (Basel) 8 (4) (2018) 200.
[61] C. Torres-Sanchez, F. Al Mushref, M. Norrito, K. Yendall, Y. Liu, P.P. Conway, The effect of pore size and porosity on mechanical properties and biological response of porous titanium scaffolds, Mater. Sci. Eng.: C 77 (2017) 219–228.
[62] A. Entezari, I. Roohani, G. Li, C.R. Dunstan, P. Rognon, Q. Li, X. Jiang, H. Zreiqat, Architectural design of 3D printed scaffolds controls the volume and functionality of newly formed bone, Adv Healthc Mater 8 (1) (2019) 1801353.
[63] T. Albrektsson, A. Wennerberg, On osseointegration in relation to implant surfaces, Clin Implant Dent Relat Res 21 (2019) 4–7.
[64] Y. Liu, B. Rath, M. Tingart, J. Eschweiler, Role of implants surface modification in osseointegration: a systematic review, J. Biomed. Mater. Res. Part A 108 (3) (2020) 470–484.
[65] K. Kieswetter, Z. Schwartz, T. Hummert, D. Cochran, J. Simpson, D. Dean, B. Boyan, Surface roughness modulates the local production of growth factors and cytokines by osteoblast-like MG-63 cells, J. Biomed. Mater. Res.: An Official Journal of The Society for Biomaterials and The Japanese Society for Biomaterials 32 (1) (1996) 55–63.
[66] V. Weißmann, P. Drescher, H. Seitz, H. Hansmann, R. Bader, A. Seyfarth, A. Klinder, A. Jonitz-Heincke, Effects of build orientation on surface morphology and bone cell activity of additively manufactured Ti6Al4V specimens, Materials (Basel) 11 (6) (2018) 915.
[67] S.A. Yavari, S. Ahmadi, J. van der Stok, R. Wauthlé, A. Riemslag, M. Janssen, J. Schrooten, H. Weinans, A.A. Zadpoor, Effects of bio-functionalizing surface treatments on the mechanical behavior of open porous titanium biomaterials, J Mech Behav Biomed Mater 36 (2014) 109–119.
[68] R. Asri, W. Harun, M. Samykano, N. Lah, S. Ghani, F. Tarlochan, M. Raza, Corrosion and surface modification on biocompatible metals: a review, Mater. Sci. Eng.: C 77 (2017) 1261–1274.
[69] R. Huiskes, H. Weinans, B. Van Rietbergen, The relationship between stress shielding and bone resorption around total hip stems and the effects of flexible materials, Clin. Orthop. Relat. Res. (1992) 124–134.
[70] J.D. Bobyn, E.S. MORTIMER, A.H. GLASSMAN, C.A. ENGH, J.E. MILLER, C.E. BROOKS, Producing and avoiding stress shielding: laboratory and clinical observations of noncemented total hip arthroplasty, Clin. Orthop. Relat. Res. (1976-2007) 274 (1992) 79–96.
[71] R. Hedayati, S. Janbaz, M. Sadighi, M. Mohammadi-Aghdam, A. Zadpoor, How does tissue regeneration influence the mechanical behavior of additively manufactured porous biomaterials? J Mech Behav Biomed Mater 65 (2017) 831–841.
[72] F. Li, J. Li, G. Xu, G. Liu, H. Kou, L. Zhou, Fabrication, pore structure and compressive behavior of anisotropic porous titanium for human trabecular bone implant applications, J Mech Behav Biomed Mater 46 (2015) 104–114.
[73] S.A. Goldstein, The mechanical properties of trabecular bone: dependence on anatomic location and function, (1987).
[74] J.-.Y. Rho, L. Kuhn-Spearing, P. Zioupos, Mechanical properties and the hierarchical structure of bone, Med Eng Phys 20 (2) (1998) 92–102.
[75] M. Silva, E.F. Shepherd, W.O. Jackson, F.J. Dorey, T.P. Schmalzried, Average patient walking activity approaches 2 million cycles per year: pedometers under-record walking activity, J Arthroplasty 17 (6) (2002) 693–697.
[76] V.S. Nikolaou, N. Efstathopoulos, G. Kontakis, N.K. Kanakaris, P.V. Giannoudis, The influence of osteoporosis in femoral fracture healing time, Injury 40 (6) (2009) 663–668.
[77] Y. Liu, H. Wang, S. Li, S. Wang, W. Wang, W. Hou, Y. Hao, R. Yang, L. Zhang, Compressive and fatigue behavior of beta-type titanium porous structures fabricated by electron beam melting, Acta Mater 126 (2017) 58–66.
[78] W. Zhang, P. Soman, K. Meggs, X. Qu, S. Chen, Tuning the poisson's ratio of biomaterials for investigating cellular response, Adv Funct Mater 23 (25) (2013) 3226–3232.
[79] H.J. Choi, J.J. Lee, Y.J. Park, J.-.W. Shin, H.-.J. Sung, J.W. Shin, Y. Wu, J.K. Kim, MG-63 osteoblast-like cell proliferation on auxetic PLGA scaffold with mechanical stimulation for bone tissue regeneration, Biomater Res 20 (1) (2016) 33.